Pd–MgNi$_x$ nanospheres/black-TiO$_2$ porous films with highly efficient hydrogen production by near-complete suppression of surface recombination

Jianyun Zheng [a,*], Shanhu Bao [a], Xiaoli Zhang [a,b], Haibo Wu [a], Rongxiang Chen [a,b], Ping Jin [a,c,**]

[a] State Key Laboratory of High Performance Ceramics and Superfine Microstructure, Shanghai Institute of Ceramics, Chinese Academy of Sciences, Dingxi Rd. 1295, Changning District, Shanghai 200050, China
[b] Graduate School of Chinese Academy of Sciences, Beijing 100049, China
[c] Materials Research Institute for Sustainable Development, National Institute of Advanced Industrial Science and Technology (AIST), 2266-98 Shimoshidami, Moriyama-ku, Nagoya 463-8560, Japan

ARTICLE INFO

ABSTRACT

Hydrogen generated from solar-driven photocatalytic water splitting has the potential to be a clean, sustainable and abundant energy source. Herein, we demonstrate that Pd–MgNi$_x$ nanospheres/black-TiO$_2$ porous films serve as a highly efficient and convenient catalyst for photogeneration of hydrogen from water. Near-complete suppression of surface recombination ensures the excellent photocatalytic activity of Pd–MgNi$_x$ nanospheres/black-TiO$_2$ porous films, corresponding to high hydrogen production rates (34.93 mmol h^{-1} g^{-1}). The result is promising for overall solar water splitting in a simple system, and is encouraging for application of this surface modification strategy to other candidate semiconductors.

© 2015 Elsevier B.V. All rights reserved.

1. Introduction

Solar-to-chemical energy conversion, which does not emit greenhouse gases and only obtain clean and storable molecular fuels such as hydrogen (H$_2$), is the ultimate goal for scientists in the field of energy generation [1]. Driven by increasing energy needs, decreasing fossil fuel resources and environmental concerns of nuclear energy, the search for utilization of solar energy to produce H$_2$ from water is necessary to carry out. In nature, cyanobacteria performed a way to split water into H$_2$ and oxygen (O$_2$) by sunlight around 3 billion years ago [2]. The energy-conversion efficiency of natural photosynthesis can reach about 7% under optimum conditions, although an efficiency of less than 1% is usually expected for nearly all forms of life on earth [3,4]. Currently, mankind has been trying to emulate natural photosynthesis through some artificial materials, hoping to find an alternative for nonrenewable and polluting fossil fuels [5]. Since the first report in 1972 by Fujishima and Honda that TiO$_2$ could act as a photochemical water-splitting catalyst [6], over 100 photocatalysts have been discussed [7]. Among the various types of photocatalysts, TiO$_2$ has been extensively studied for several decades due to its abundance, nontoxicity, and stability. Furthermore, as an efficient photocatalyst for splitting water, TiO$_2$ has a conduction band minimum that is higher than the H$_2$/H$_2$O level and a valence band maximum that is lower than the H$_2$O/O$_2$ level [8].

Photocatalytic reactions in solid-state catalysis are determined primarily by three reaction processes: (i) light-harvesting processes [8,9], (ii) charge generation and separation processes [10,11], and (iii) catalytic reaction processes [12–14]. The overall efficiency is determined by the balance of thermodynamics and kinetics of these processes. In recent decades, intensive work for these processes has been undertaken, both experimentally and theoretically, to improve the performance of the widely used TiO$_2$-based catalysts. Regarding to narrowing the band gap of TiO$_2$, much research has focused on selective doping of metallic, nonmetallic and mixed elements (e.g. C, N, Fe) into the lattice of TiO$_2$ [15]. However, problems such as thermal instability and increased carrier recombination centers pose significant limitations for this strategy [16]. Recently,

* Corresponding author.
** Corresponding author at: State Key Laboratory of High Performance Ceramics and Superfine Microstructure, Shanghai Institute of Ceramics, Chinese Academy of Sciences, Dingxi Rd. 1295, Changning District, Shanghai 200050, China.
   E-mail addresses: wetrainzjy@163.com (J. Zheng), p-jin@mail.sic.ac.cn (P. Jin).
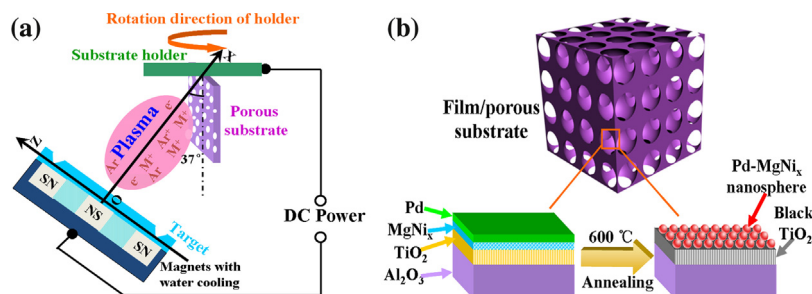
Fig. 1. (a) Schematic diagram of the deposition configuration, (b) schematic illustration for the preparation of PMNBTPF grown on the α-Al_2O_3 porous ceramic wafers.

black-TiO_2 (TiO_{2-y} or reduced TiO_2), which involves the Ti^{3+} or oxygen vacancy [17], has been demonstrated to possess the large solar absorption and exhibit substantial solar-driven photocatalytic activities [18,19]. Therefore, the black-TiO_2 can offer the essential advantage in absorbing visible and infrared light. However, issues of limited specific surface area and recombination of electron-hole should be further addressed before practical application of black-TiO_2.

On the other hand, directly constructing 3D architecture on porous substrates can partially overcome the above issues, thereby leading to a dramatic improvement in the water-splitting per-

formance of the active materials [20–22]. Compared to the conventional 2D planar architecture, photocatalysts based on 3D porous architecture can show several critical advantages, such as facilitating mass transfer of the water and H_2, and increasing the active surface area [23]. Recent work has confirmed the great benefit of 3D architecture in enhancing the photocatalytic activity of TiO_2 [24,25]. Thus, 3D black-TiO_2 films are anticipated to show excellent photocatalytic water-splitting performance. In addition to increasing the surface area, it is more important to optimize the photogenerated electron-hole separation characteristics over the black-TiO_2 surface. Notably, suitable cocatalysts/black-TiO_2 system
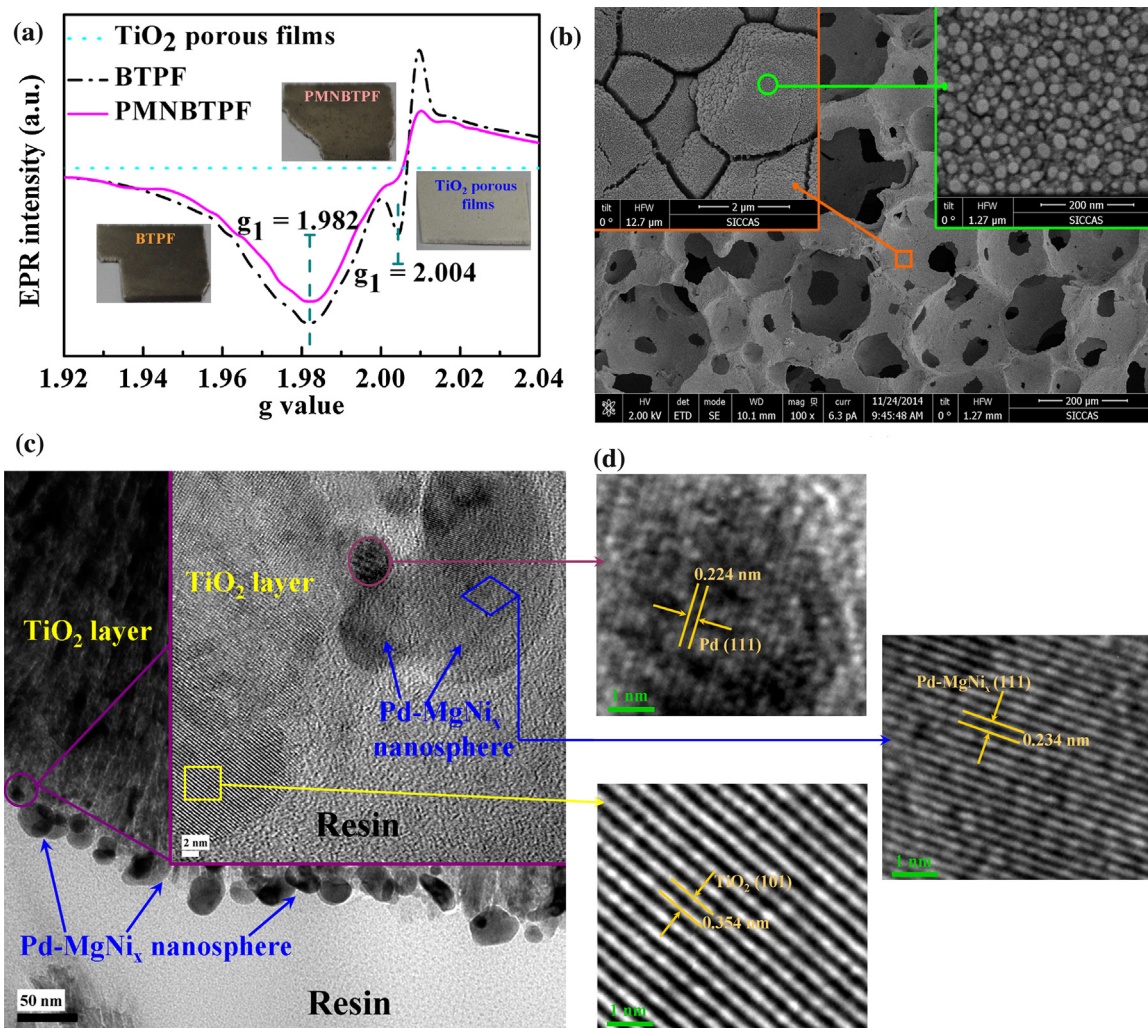

Fig. 2. (a) EPR spectra of pristine TiO_2 porous film, BTPF and PMNBTPF (the insets show the photographs of these films). (b) Top view FESEM image of PMNBTPF (the left and right insets correspond to the orange square and green ring in the relevant image with high magnification, respectively). (c) Cross-sectional TEM image of PMNBTPF (the inset is the relevant magnification image by HRTEM). (d) High magnification images corresponding to the marked area in the inset of Fig. 2c.

Table 1

Deposition conditions of each layer to produce the multilayer film. In table, "Mg–Ni" is represented as the co-sputtering of Mg and Ni targets. "40–16" is corresponding to the work power of each target during co-sputtering process.

Layer	Work power (W)	Target	Time (min)	Pressure (Pa)	Ar flow rate (sccm)	O_2 flow rate (sccm)
TiO_2	700	Ti	180	1.0	35	5
$MgNi_x$	40–16	Mg–Ni	1/2	0.5	40	0
Pd	20	Pd	2/3	0.5	40	0

can effectively reduce the photogenerated electron-hole recombination because cocatalysts are able to serve as electron (hole) sinks to expedite interfacial electron (hole) transfer [26,27]. The development of cocatalysts in photocatalytic reactions goes through from single metal to multi-component cocatalysts including noble metal, transition metal, and/or metal oxide etc. Two or more components usually result in multifunctional or synergetic effects in photocatalysis, which may greatly enhance the photocatalytic activity [28]. Through these investigations, it is reasonably assumed that the easy accessibility of multi-component cocatalysts/black-TiO_2 based 3D films can help its commercial production. Mg-Ni alloy thin films are well known materials for absorption and desorption of hydrogen at room temperature in atmosphere [29], however, the materials are less discussed in a catalyst system.

Here, we use a simple α-Al_2O_3 porous ceramic wafer as the raw sources to synthesize Pd–MgNi_x nanospheres/black-TiO_2 porous films (PMNBTPF) for efficient water splitting into H_2. The hierarchical porous morphology of ceramic wafer and self-doped Ti^{3+} are retained in the obtained systems to offer more absorption and reaction sites for enhanced catalytic reactions. Metals (Pd and MgNi_x) are the electron transfer mediator, contributing to the enhancement of electron-hole separation and interfacial charge transfer. Moreover, metal Pd and partially oxidized MgNi_x alloy acted as the reduction and oxidation sites can further avoid the surface charge recombination. The analysis of the photoluminescence (PL) emission spectra shows nearly complete elimination of surface electron-hole recombination for PMNBTPF. Compared with pure black-TiO_2 porous films (BTPF, its structure shown in Supporting information), PMNBTPF can yield over an order of magnitude improvement in the effectiveness of solar-driven photocatalytic water-splitting (34.93 mmol h^{-1} g^{-1} of hydrogen production rates).

2. Experimental section

2.1. Sample preparation

The α-Al_2O_3 porous ceramic wafers with around 1.15 mm thickness were applied as the substrates. Firstly, Pd/MgNi_x/TiO_2 multilayer film with 3D architecture was deposited using a direct current magnetron sputtering (dcMS) system (Shenyang Tengao Vacuum Technology Co. Ltd., JSS-600) to sputter planar round metal targets (purity > 99.5 wt.%) in pure Ar (99.99%) or mixed Ar/O_2 (99.99%) atmosphere at room temperature. The schematic diagram of the deposition configuration is shown in Fig. 1a. Using a load-lock system, the base pressure of the deposition chamber was kept at 5.0×10^{-4} Pa. Thereafter, the power was charged on the metal target with injection of corresponding gas and the layer/film was deposited. Details of the deposition conditions of each layer are listed in Table 1. After deposition, the fresh film was annealed in vacuum annealing furnace at 600 °C for 5 min to form the PMNBTPF, as described in Fig. 1b.

2.2. Film characterization

The chemical composition of the film surface was analyzed by X-ray photoelectron spectroscopy (XPS) with monochromated Al Kα radiation on at a pass energy of 29.4 eV. All binding energies were referenced to the C1s peak (285.0 eV) arising from adventitious carbon. Electron paramagnetic resonance (EPR) spectra were taken on a JES FA-200 (JEOL) continuous-wave EPR spectrometer by applying an X band (9.1 GHz) and a sweeping magnetic field at 120 K. Aiming to determine the microstructure of the film, field emission scanning electron microscopy (FESEM, Magellan 400) and high-resolution transmission electron microscopy (HRTEM, Tecnai G2 F20 S-Twin) were employed to observe the surface and cross section of the film. The synchronous analysis of the component content and structure is performed by scanning transmission electron microscopy (STEM, Magellan 400) with a High Angle Annular Dark Field (HAADF) detector and energy dispersive X-ray spectroscopy (EDS). Photoluminescence (PL) spectra were measured at room temperature on a fluorescence spectrophotometer (Fls-920, Edinburgh).

2.3. Photocatalytic H_2 generation

The photocatalytic H_2 production experiments were performed in a 550 mL Pyrex glass vessel at ambient temperature and N_2 atmosphere, and two openings of the vessel were connecting a gas chromatograph (D7900P, Techcomp), as depicted in Supporting Information. An AM 1.5 solar power system was used as light irradiation source. In a typical photocatalytic experiment, 0.19 mg of catalyst subtracting from the weight of substrate was placed into an aqueous methanol solution (40 mL, 25%). Methanol was used as a sacrificial reagent to avoid the anodic reaction generating O_2 from H_2O.

3. Results and discussion

To determine the relationship between the black-TiO_2 and presence of Ti^{3+}, low temperature EPR spectra were recorded in Fig. 2a. BTPF and PMNBTPF with dark color both gave rise to a very strong EPR signal, while no signal was seen for the pristine TiO_2 porous film (white, its preparation shown in Supporting Information). It is well-known that the major features in this spectrum ($g_1 = 1.982$ and $g_2 = 2.004$) belong to the paramagnetic Ti^{3+} centers in a distorted rhombic oxygen ligand field [30,31] and single electron-trapped oxygen vacancies (SETOVs, or reduced O_2^-) [32,33], respectively. The SETOVs usually play the role of a recombination center of photogenerated electron-hole resulting in a bad photocatalytic behavior. Compared with BTPF with black, PMNBTPF with more light color (dark gray in Fig. 2a) only showed a slightly weaker intensity of EPR signal at $g_1 = 1.982$. On the basis of these results, the presence of rhombic Ti^{3+} is unambiguously verified in the PMNBTPF, which is a key factor in the excellent stability of our sample. As regards the absence of EPR signal at $g_2 = 2.004$ for PMNBTPF, it is rational reason that the black-TiO_2 layer capped by Pd–MgNi_x nanospheres would be difficult to adsorb atmospheric O_2 to form O_2^-. Fig. 2b displays the top view FESEM images of PMNBTPF with different magnification. The observed images of PMNBTPF revealed a 3D porous structure originated from α-Al_2O_3 substrate. Moreover, Pd–MgNi_x nanospheres with a diameter of about 20 nm loading on the black-TiO_2 layer were highly dispersed and nearly free-stacked. In order to further uncover the microstructure, PMNBTPF was examined by TEM and HRTEM, as shown in
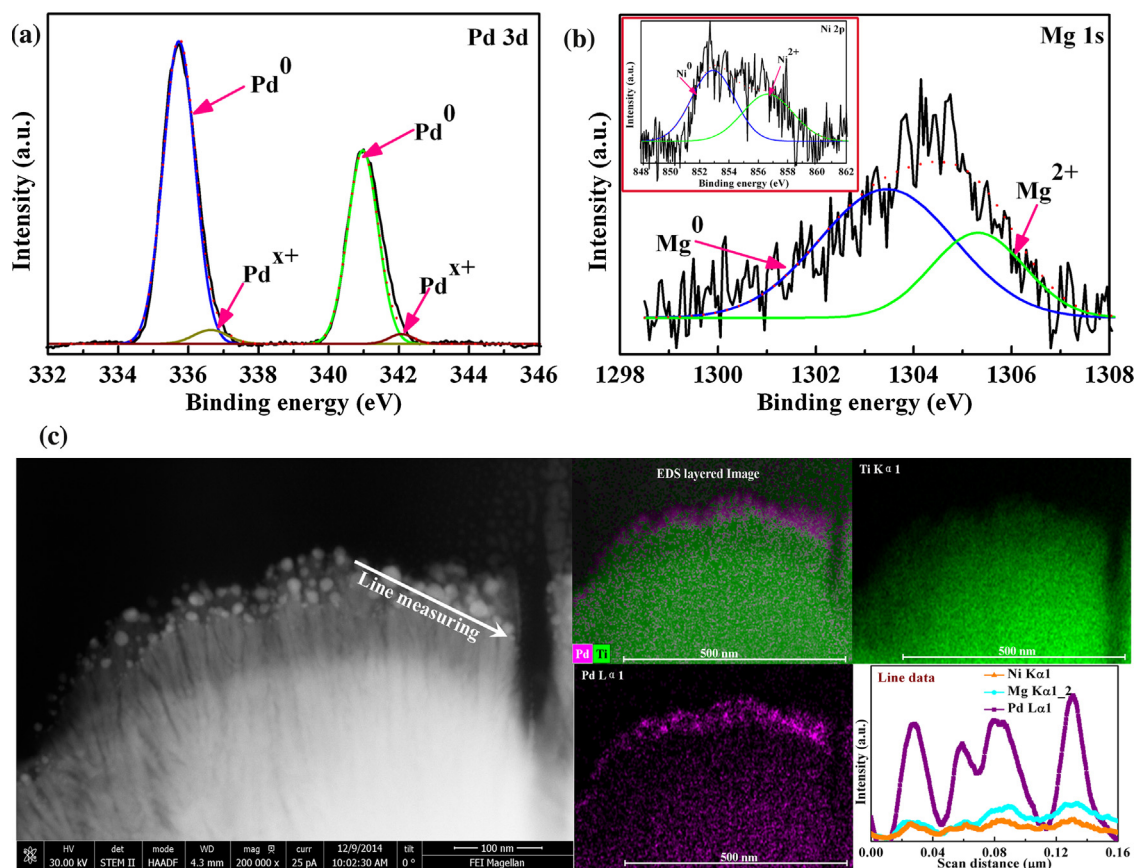
Fig. 3. XPS analysis of PMNBTPF: (a) Pd 3d spectra; (b) Mg 1s spectra (the inset is Ni 2p spectra). (c) HAADF-STEM image with corresponding elemental distribution map and EDS-line measurements for PMNBTPF.

Fig. 2c and d. The black-TiO_2 layer had a dense and continuous columnar structure and the layer thickness was 500 nm. Pd–MgNi$_x$ nanospheres on the surface of black-TiO_2 layer were as a single layer with around 20 nm thickness, in line with FESEM images. The HRTEM images gave some lattice fringes with spacing of 0.354 nm, 0.224 nm and 0.234 nm on the film surface, which can be indexed as the (1 0 1) plane of anatase TiO_2, the (1 1 1) plane of face-centered cubic (fcc) structures of Pd and Pd–MgNi$_x$ [34,35], respectively. It should be pointed out that Pd–MgNi$_x$ nanospheres made up of the pure Pd nanospheres and the Pd–MgNi$_x$ alloy nanospheres, where the size of the former was smaller than that of the later. The well-dispersed and small-sized Pd–MgNi$_x$ nanospheres are desired to enhance the photocatalytic activity concerning the strong metal-support interaction [36,37].

XPS is a powerful tool to examine the change of surface chemical bonding. It is briefly outlined that the Ti 2p XPS spectrum of PMNBTPF was almost identical for that of BTPF, which was broader at lower binding energy than pristine TiO_2 porous film because of the appearance of Ti^{3+} (shown in Supporting information) [38]. Fig. 3a is typical XPS spectrum of Pd 3d of PMNBTPF containing two group peaks corresponding to Pd 3d$_{5/2}$ and Pd 3d$_{3/2}$. After implementing the deconvolution with Lorentzian-Gaussian distribution function, the Pd 3d$_{5/2}$ spectrum displayed two peaks at 335.7 eV and 336.6 eV, which are assigned to metallic Pd (Pd^0) and intermediate species PdO$_{x/2}$ (Pd^{x+}), respectively [39,40]. Generally speaking, a very thin location or island (monolayer range) covering a Pd core would be prone to yield tiny amounts of PdO$_{x/2}$ in the air. In addition, XPS spectra of Mg 1s and Ni 2p of PMNBTPF are shown in Fig. 3b. The peak positions of the metallic state and oxide state of Mg was reported as 1303.3 eV and 1305.3 eV for Mg 1s spectrum,

respectively [41]. This means that MgO existed at the surface of Pd–MgNi$_x$ nanospheres. Meanwhile, Ni 2p$_{3/2}$ peaks at 852.9 eV and 856.6 eV could be attributed to metallic state and hydroxide state of Ni, respectively [42]. Apparently, oxidized Mg or Ni should be an integrated part of MgNi$_x$ alloy, because the peak with the high intensity located at around 1305.3 eV or 856.6 eV.

To further investigate the content and distribution of composition, STEM image coupled with EDS mapping and line data for the PMNBTPF are exhibited in Fig. 3c. According to the EDS mapping, Pd nanospheres were supported on the black-TiO_2 layer, while MgNi$_x$ alloy can be hardly recognized owing to its low content leading to weak signal as well as distinct noise signal (shown in supporting information). However, elemental distribution by the spectrum line mode indicates that the variation trend of Pd and MgNi$_x$ was almost consistent, which implies the existence of Pd–MgNi$_x$ nanospheres. Besides, the atom ratio of Pd, Mg and Ni for the nanospheres is around 17:2:1 calculated by EDS data, in agreement with the XPS results.

The PL emission spectra are useful to understand the efficiency of the charge carrier trapping, migration, transfer and separation and to estimate the fate of photogenerated electrons and holes in semiconductor since PL emission results from the recombination of free carriers [43]. The PL properties of PMNBTPF were compared to that of BTPF, as presented in Fig. 4a. For BTPF, three main emission peaks were located at about 387 nm, 450 nm, and 465 nm labeled by dash lines, which are equivalent to 3.20 eV, 2.76 eV, and 2.67 eV, respectively. The relatively weak PL peak at about 387 nm is usually ascribed to the emission of bandgap transition with the energy of light approximately equal to the bandgap energy of anatase (387.5 nm). The strong peaks observed in the wavelength range
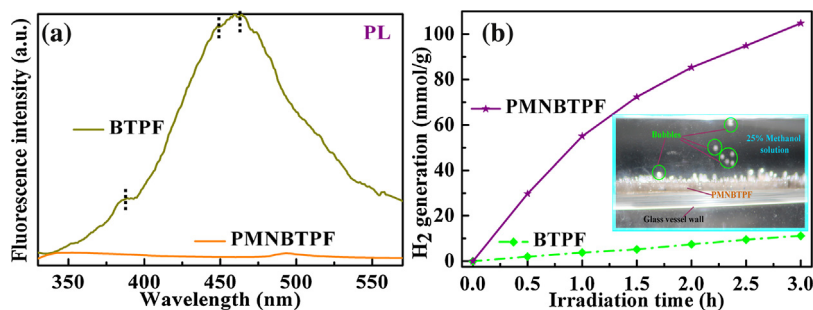
Fig. 4. (a) PL spectra of BTPF and PMNBTPF. (b) Comparison of the photocatalytic production of H_2 from methanol aqueous solution for BTPF and PMNBTPF (the inset is photographic illustration of direct photocatalytic water splitting under simulated solar light).

from 440 to 500 nm result from the recombination of electrons and holes at surface trap sites (oxygen vacancies). Compared with BTPF, a considerable fluorescence quenching was observed in PMNBTPF. Only a tiny peak at 494 nm for PMNBTPF is derived from bound excitons [44]. The quenching of fluorescence indicates a close contact between black-TiO_2 layer and Pd–$MgNi_x$ nanospheres and a quick transfer of photogenerated electrons from black-TiO_2 to Pd–$MgNi_x$ via the favorable [45]. Besides, it is another sound reason for the decrease of fluorescence that metallic Pd and oxidized MgNi alloy can serve as electron and hole sinks to promote the separation of the charge carriers [46].

Generally, a near-complete suppression of surface recombination of electrons and holes is often associated with an excellent photocatalytic water-splitting behavior [47,48]. The H_2 generation of BTPF and PMNBTPF is illustrated in Fig. 4b. Control experiments showed no appreciable H_2 production in the absence of either irradiation or photocatalyst, suggesting that H_2 was yielded by photocatalytic reactions on TiO_2-based films under solar illumination. Under the solar light irradiation, a lot of bubbles collected on the surface of PMNBTPF, and then coalesced to grow until rising, as observed in the inset of Fig. 4b. As reported in previous work, the coverage of the film surface by the gas bubbles directly reduced the contact between the reaction solution and the film and blocked the electron transfer. Thus, the increase of the big bubbles gives rise to the decrease of hydrogen production when the illumination time increases. In order to improve the phenomenon, we will try to minimize the bubble size and reduce the residence time of bubble staying in the film surface in future study. Fortunately, even if under this conditions, the PMNBTPF steadily produced H_2 gas up to 34.93 mmol h^{-1} g^{-1}, almost ten times higher than the BTPF (3.72 mmol h^{-1} g^{-1}). Our PMNBTPF displays a noticeable improvement, which even surpasses the best ranks ($\approx$10 mmol h^{-1} g^{-1}) among the TiO_2-based photocatalysts [18,19]. The energy conversion efficiency for solar hydrogen production, defined as the ratio between the energy of solar-generated H_2 and the energy of the incident sunlight, reached around 83% for PMNBTPF.

To further evaluate the photocatalytic efficiency of PMNBTPF, the turnover frequency (TOF) and turnover number (TON) were calculated by their definitions. TOF is equal to the number of reactant molecules converted per minute per catalytic site for given reaction conditions, and TON results from multiplication of TOF and the lifetime of the catalyst [49]. In this work, the active sites for PMNBTPF should be distributed at half the number of the Pd–$MgNi_x$ nanospheres. On account of the morphology of the nanospheres, we propose roughly that the nanoshperes are uniform balls with a diameter of 20 nm. Thus, during the photocatalytic water-splitting, the number of active sites for PMNBTPF are about 7.89×10^{18} obtained using the related formula (shown in Supporting Information). After irradiated by solar light for 3 h, the values of TOF and TON are 0.73×10^{-3} s^{-1} and 7.91 for PMNBTPF. Exhilaratingly, the sample was very stable because they almost kept
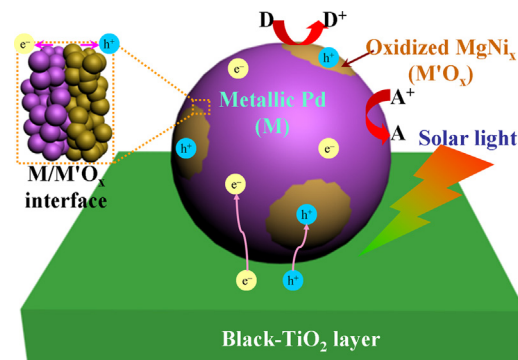

Fig. 5. Schematic description of the proposed mechanisms of electron-hole separation and photocatalytic reaction on PMNBTPF.

up the same H_2 generation in several photocatalysis cycles in a month (shown in Supporting Information). In addition to hydrogen production from water splitting, we examined photocatalytic decomposition of pure rhodamine B (RhB) (0.6×10^{-3} M, 20 mL) and a mixture solution (20 mL) of RhB (0.2×10^{-3} M) and methyl orange (MO) (0.2×10^{-3} M) using PMNBTPF as the photocatalysts to further evaluate the photocatalytic activity of the films (shown in Supporting Information). Photodegradation of RhB and mixture solution was nearly completed after 120 min for PMNBTPF. All these investigations demonstrate that PMNBTPF promises an excellent photocatalytic activity.

On the basis of the above results, the possible mechanisms for high H_2 production are proposed as the following, which is schematically exhibited in Fig. 5. Three processes would occur: (i) the incident photons are absorbed by black-TiO_2 layer to generate the photoexcited electron-hole pairs over the surface of TiO_2, (ii) the electrons and holes are transferred from the black-TiO_2 layer into the Pd–$MgNi_x$ nanosphere, (iii) oxidation reaction and reduction reaction take place on oxidized $MgNi_x$ and metallic Pd by holes and electrons, respectively, resulting in the production of H_2 gas. First of all, the metallic particles loading on black-TiO_2 layer can help the electron-hole separation and improve the quantum yield by accelerating the removal and transfer of electrons [50,51]. Since the Fermi level of metallic particles (i.e. Pd, Ni) is lower than that of black-TiO_2 [26,52], electron transfer from TiO_2 to metallic particle in process (ii) is reasonable. Accordingly, oxidized $MgNi_x$ regions are able to trap holes very well [53]. Although TiO_2 itself could act as the oxidation sites, when oxidized $MgNi_x$ locates on the surface of TiO_2, the holes would be prior to transferring to oxidized $MgNi_x$. Therefore in this case, metallic Pd and oxidized $MgNi_x$ should be the main reduction and oxidation sites for H_2 evolution and photocatalytic methanol reforming. Because of the presence of little CO and O_2, it is believed that the good oxidation ability of PMNBTPF

can give rise to the total oxidation of methanol to CO_2 rather than CO. The photocatalytic reaction proceeds as follows [28]:

$$HCOOH + 2h^+ \rightarrow CO_2 + 2H^+ \tag{1}$$

$$2H^+ + 2e^- \rightarrow H_2 \tag{2}$$

Apparently, to complete the whole reaction, the proton (H^+) is transported from the oxidation sites to the reduction sites. Thus, the photocatalytic reactions are very efficient and fast for the oxidation and reduction sites in the same nanospheres with intimate contact. In addition, it is necessary to point out that methanol is hardly dehydrogenated to produce H_2 and formaldehyde (HCHO). Because the characteristic carbonyl C—O bond vibrations of HCHO is difficult to be observed in Fourier transform infrared (FTIR) spectra of the aqueous methanol solution reacted by Pd–MgNi$_x$ nanospheres/black-TiO$_2$ porous films (shown in Supporting Information).

4. Conclusion

In conclusion, a novel Pd–MgNi$_x$ nanospheres/black-TiO$_2$ porous film was deposited by dcMS and annealed at high temperature. The resultant composite film showed an excellent photocatalytic activity toward H_2 production from water-splitting under solar light irradiation, as compared with black-TiO$_2$ porous film. The enhanced photoactivity lay crucially on the contribution role of unproductive surface electron-hole recombination. A synergetic effect between the transfer of charge carriers and the oxidation and reduction reaction occurring in different sites leaded to the near-complete suppression of surface recombination.

Acknowledgements

Appendix A. Supplementary data

Supplementary data associated with this article can be found, in the online version, at http://dx.doi.org/10.1016/j.apcatb.2015.10.031.

References

[1] Y. Tachibana, L. Vayssieres, J.R. Durrant, Nat. Photonics 6 (2012) 511–518.
[2] D.J. Des Marais, Science 289 (2000) 1703–1705.
[3] J. Barber, Chem. Soc. Rev. 38 (2009) 185–196.
[4] R.E. Blankenship, D.M. Tiede, J. Barber, G.W. Brudvig, G. Fleming, M. Ghirardi, M.R. Gunner, W. Junge, D.M. Kramer, A. Melis, T.A. Moore, C.C. Moser, D.G. Nocera, A.J. Nozik, D.R. Ort, W.W. Parson, R.C. Prince, R.T. Sayre, Science 332 (2011) 805–809.
[5] A. Kay, I. Cesar, M. Gratzel, J. Am. Chem. Soc. 128 (2006) 15714–15721.
[6] A. Fujishima, K. Honda, Nature 238 (1972) 37.
[7] F.E. Osterloh, Chem. Mater. 20 (2008) 35–54.
[8] S.U.M. Khan, M. Al-Shahry, W.B. Ingler, Science 297 (2002) 2243–2245.
[9] S. Sato, Chem. Phys. Lett. 123 (1986) 126–128.
[10] A. Galinska, J. Walendziewski, Energy Fuel 19 (2005) 1143–1147.
[11] S. Kment, P. Kluson, V. Stranak, P. Virostko, J. Krysa, M. Cada, J. Pracharova, M. Kohout, M. Morozova, P. Adamek, Z. Hubicka, Electrochim. Acta 54 (2009) 3352–3359.
[12] J. Nowotny, C.C. Sorrell, T. Bak, L.R. Sheppard, Sol. Energy 78 (2005) 593–602.
[13] J.G. Yu, Y.R. Su, B. Cheng, Adv. Funct. Mater. 17 (2007) 1984–1990.
[14] N.Q. Wu, J. Wang, D. Tafen, H. Wang, J.G. Zheng, J.P. Lewis, X.G. Liu, S.S. Leonard, A. Manivannan, J. Am. Chem. Soc. 132 (2010) 6679–6685.
[15] R. Daghrir, P. Drogui, D. Robert, Ind. Eng. Chem. Res. 52 (2013) 3581–3599.
[16] F. Zuo, L. Wang, T. Wu, Z.Y. Zhang, D. Borchardt, P.Y. Feng, J. Am. Chem. Soc. 132 (2010) 11856–11857.
[17] Z.K. Zheng, B.B. Huang, J.B. Lu, Z.Y. Wang, X.Y. Qin, X.Y. Zhang, Y. Dai, M.H. Whangbo, Chem. Commun. 48 (2012) 5733–5735.
[18] X.B. Chen, L. Liu, P.Y. Yu, S.S. Mao, Science 331 (2011) 746–750.
[19] Z. Wang, C.Y. Yang, T.Q. Lin, H. Yin, P. Chen, D.Y. Wan, F.F. Xu, F.Q. Huang, J.H. Lin, X.M. Xie, M.H. Jiang, Adv. Funct. Mater. 23 (2013) 5444–5450.
[20] P. Simon, Y. Gogotsi, Nat. Mater. 7 (2008) 845–854.
[21] Y.H. Chang, C.T. Lin, T.Y. Chen, C.L. Hsu, Y.H. Lee, W.J. Zhang, K.H. Wei, L.J. Li, Adv. Mater. 25 (2013) 756–760.
[22] J. Kibsgaard, Z.B. Chen, B.N. Reinecke, T.F. Jaramillo, Nat. Mater. 11 (2012) 963–969.
[23] R.M. Mohamed, E.S. Baeissa, Appl. Catal. A: Gen. 464 (2013) 218–224.
[24] J.S. Luo, S.K. Karuturi, L. Liu, L.T. Su, A.I.Y. Tok, H.J. Fan, Sci. Rep. UK 2 (2012) 451.
[25] E.M. Neville, J.M.D. MacElroy, K.R. Thampi, J.A. Sullivan, J. Photoch. Photobio. A 267 (2013) 17–24.
[26] X.Y. Pan, Y.J. Xu, J. Phys. Chem. C 117 (2013) 17996–18005.
[27] D. Duonghong, E. Borgarello, M. Gratzel, J. Am. Chem. Soc. 103 (1981) 4685–4690.
[28] Y. Ma, R.F. Chong, F.X. Zhang, Q. Xu, S. Shen, H.X. Han, C. Li, Phys. Chem. Chem. Phys. 16 (2014) 17734–17742.
[29] T.J. Richardson, J.L. Slack, R.D. Armitage, R. Kostecki, B. Farangis, M.D. Rubin, Appl. Phys. Lett. 78 (2001) 3047–3049.
[30] J.Y. Zheng, S.H. Bao, Y. Guo, P. Jin, ACS Appl. Mater. Interfaces 6 (2014) 5940–5946.
[31] V.M. Khomenko, K. Langer, H. Rager, A. Fett, Phys. Chem. Miner. 25 (1998) 338–346.
[32] M. Anpo, M. Che, B. Fubini, E. Garrone, E. Giamello, M.C. Paganini, Top Catal. 8 (1999) 189–198.
[33] J.M. Cho, W.J. Yun, J.K. Lee, H.S. Lee, W.W. So, S.J. Moon, Y. Jia, H. Kulkarni, Y. Wu, Appl. Phys. A: Mater. 88 (2007) 751–755.
[34] T. Teranishi, M. Miyake, Chem. Mater. 10 (1998) 594–600.
[35] M. Ponthieu, J.F. Fernandez, F. Cuevas, J.R. Ares, F. Leardini, J. Bodega, C. Sanchez, J. Alloys Compd. 548 (2013) 96–104.
[36] R. Camposeco, S. Castillo, I. Mejia-Centeno, J. Navarrete, J. Marin, Mater. Charact. 95 (2014) 201–210.
[37] F. Niu, S.Q. Li, Y.C. Zong, Q. Yao, J. Phys. Chem. C. 118 (2014) 19165–19171.
[38] J.Y. Zheng, S.H. Bao, Y. Guo, P. Jin, ACS Appl. Mater. Interfaces 6 (2014) 1351–1355.
[39] S. Gatla, N. Madaan, J. Radnik, V.N. Kalevaru, M.M. Pohl, A. Martin, U. Bentrup, A. Bruckner, J. Catal. 297 (2013) 256–263.
[40] B. Tapin, F. Epron, C. Especel, B.K. Ly, C. Pinel, M. Besson, ACS Catal. 3 (2013) 2327–2335.
[41] K. Tajima, Y. Yamada, S.H. Bao, M. Okada, K. Yoshimura, Jpn. J. Appl. Phys. 48 (2009) 102402.
[42] S. Oswald, W. Bruckner, Surf. Interface Anal. 36 (2004) 17–22.
[43] J.G. Yu, L.F. Qi, M. Jaroniec, J. Phys. Chem. C 114 (2010) 13118–13125.
[44] J.G. Yu, L. Yue, S.W. Liu, B.B. Huang, X.Y. Zhang, J. Colloid Interface Sci. 334 (2009) 58–64.
[45] N. Hintsho, L. Petrik, A. Nechaev, S. Titinchi, P. Ndungu, Appl. Catal. B: Environ. 156 (2014) 273–283.
[46] A. Kudo, Y. Miseki, Chem. Soc. Rev. 38 (2009) 253–278.
[47] T.F. Yeh, C.Y. Teng, S.J. Chen, H.S. Teng, Adv. Mater. 26 (2014) 3297.
[48] G.C. Xie, K. Zhang, B.D. Guo, Q. Liu, L. Fang, J.R. Gong, Adv. Mater. 25 (2013) 3820–3839.
[49] S. Kozuch, J.M.L. Martin, ACS Catal. 2 (2012) 2787–2794.
[50] C.C. Ling, Q.Z. Xue, Z.D. Han, Z.Y. Zhang, Y.G. Du, Y.M. Liu, Z.F. Yan, Sensor. Actuat. B: Chem. 205 (2014) 255–260.
[51] A. Tanaka, K. Fuku, T. Nishi, K. Hashimoto, H. Kominami, J. Phys. Chem. C 117 (2013) 16983–16989.
[52] Y.H. Liu, Z.L. Wang, W.B. Fan, Z.R. Geng, L.B. Feng, Ceram. Int. 40 (2014) 3887–3893.
[53] K. Domen, A. Kudo, T. Onishi, J. Catal. 102 (1986) 92–98.